# Holocene sea-level history from the southern Bohai Sea coast, China
## Far-field GIA processes and an associated mid-Holocene sea-level highstand

Tian, Lizhu; Vermeersen, Bert L.; Wang, Fu; Li, Jianfen; Wang, Hong

**DOI**
10.1016/j.quascirev.2024.109166

**Publication date**
2025

**Document Version**
Final published version

**Published in**
Quaternary Science Reviews

Quaternary Science Reviews 351 (2025) 109166

Contents lists available at ScienceDirect

Quaternary Science Reviews

journal homepage: www.elsevier.com/locate/quascirev

# Holocene sea-level history from the southern Bohai Sea coast, China: Far-field GIA processes and an associated mid-Holocene sea-level highstand

Lizhu Tian [a,b,*], Bert L. Vermeersen [b,c], Fu Wang [a], Jianfen Li [a], Hong Wang [a]

[a] Tianjin Center (North China Center of Geoscience Innovation), China Geological Survey (CGS), CGS Key Laboratory of Coast Geo-Environment and Tianjin Key Laboratory of Coast Geological Processes and Environmental Safety, Tianjin, 300170, China
[b] Department of Estuarine and Delta Systems, NIOZ Royal Netherlands Institute for Sea Research, Yerseke, the Netherlands
[c] Faculty of Civil Engineering and Geosciences, TU Delft, Delft, the Netherlands

ARTICLE INFO

Handling Editor: Dr Giovanni Zanchetta

*Keywords:*
Holocene
Sea-level change
GIA
Sea-level highstand
Foraminifera
Bohai sea

ABSTRACT

The Bohai Sea, located in the innermost part of the East Asian marginal seas, is of particular interest in the studies of relative sea level (RSL) and glacial isostatic adjustment (GIA) due to its apparent far-field position. This study analyzed six cores and one pre-existing archaeological site from the southern Bohai Sea coast, generating 11 sea-level index points (SLIPs) from supratidal, upper tidal, and mid-lower tidal flat sediments using foraminifera tests and sedimentary analysis. All SLIPs were corrected for possible self-compaction, long-term tectonic effect, and the lowering effect due to water extraction. This enabled a high-quality reconstruction of RSL changes over the age range of 9000–3000 cal a BP. The RSL rose rapidly from about −17.19 ± 1.32 m to 1.76 ± 1.32 m MSL between around 9000 and 7000 cal a BP. However, the RSL rise rates quickly decreased from around 8–10 mm/a before 8000 cal a BP to ~4mm/a by 7000 cal a BP. After 7000 cal a BP, the RSL continued to rise, reaching its peak of 2.44 ± 1.34 m MSL around 6000 cal a BP followed by a gradual decline to the present height at 3000–4000 cal a BP, with a maximum falling rate of 1.2 mm/a around 5000 cal a BP. Comparisons of the reconstructed RSL in this study with those from other non-deltaic regions, including the inner Hangzhou Bay and the surrounding coasts of western Bohai Sea, as well as with GIA predictions by ICE6G, ANU, and region-specific 'final model' reveal: (1) a significant and long-term early-to-mid Holocene continental levering effect on the southern Bohai Sea coast; (2) a close fit with the region-specific 'final model', albeit with SLIPs that fall slightly below predictions from 9000 to 8000 cal a BP and form a distinct mid-Holocene highstand above model projections after 7000 cal a BP; (3) these data-model misfits may result, in the former case, from the GIA model's Holocene ice melting history not embedding accelerated sea-level rise events, and in the latter, from the presence of a relatively strong upper mantle at the southern Bohai Sea coast, rather than the extremely weak upper mantle assumed for the Bohai Sea region.

## 1. Introduction

The rapid rise in ice-volume equivalent sea level (ESL) following the last deglaciation was driven by various melting stages of high latitude/altitude ice masses from the Last Glacial Maximum (LGM) (Clark and Mix, 2002; Lambeck et al., 2002; Bard et al., 2010; Stanford et al., 2011). This rise progressively inundated the East Asian marginal shelf (Hanebuth et al., 2000; Liu et al., 2004; Tian et al., 2017; Tam et al., 2018; Xiong et al., 2018; Wang et al., 2015). After 8000–7000 cal a BP, the rapid rise of ESL essentially ceased, showing only moderate increases (2–5 m) during the mid-to-late Holocene, with the primary source of meltwater being the Antarctic Ice Sheet (AIS) (Lambeck et al., 2014; Bradley et al., 2016; Argus et al., 2014; Bentley et al., 2014).

A mid-Holocene highstand in relative sea-level (RSL) is expected to be several meters in the Asian far-field, such as along the Malay-Thai Peninsula coast (Horton et al., 2005; Tam et al., 2018; Oliver and Terry, 2019), due to the levering effect of glacial isostatic adjustment (GIA) from the increasing water load in the ocean basin (Mitrovica and Milne, 2002). However, the debate regarding the existence of a higher-than-present mid-Holocene highstand at China's coasts has endured for decades. A mid-Holocene highstand of 1–2 m above present sea level was compiled from published sea-level index points along the

* Corresponding author. Tianjin Center (North China Center of Geoscience Innovation), China Geological Survey (CGS), CGS Key Laboratory of Coast Geo-Environment and Tianjin Key Laboratory of Coast Geological Processes and Environmental Safety, Tianjin, 300170, China.
*E-mail address:* tjtlizhu@163.com (L. Tian).

https://doi.org/10.1016/j.quascirev.2024.109166
Received 14 July 2024; Received in revised form 6 December 2024; Accepted 26 December 2024
Available online 6 January 2025

China Fujian coast from the 1980s–1990s (Zong, 2004). In contrast, in the regions of the Pearl River Delta (the South China Sea coast) and the inner Hangzhou Bay (the East China Sea coast), the RSL rose rapidly, reaching its present height by c. 7000 cal a BP, without an obvious mid-Holocene highstand, despite significant GIA effects in the early Holocene from both sites (Xiong et al., 2018, 2020). Bradley et al. (2016) doubted the reported 1–2 m mid-Holocene highstand at the Fujian coast (Zong, 2004), attributing it to possible tectonic activity near the plate margin and proposing that the absence of a highstand along China's coast may be attributed to weak upper mantle viscosity, particularly in the vicinity of the subduction zone and the Hainan Plume.

At a more northern site, such as the Bohai Sea region, based on the RSL prediction of the 'final model' of Bradley et al. (2016), which combines an optimized ESL model with a regional-specific lower mantle viscosity Earth model, a minor highstand of about 0.5 m was still generated by the model during the period of 7000 to 5000 cal a BP. On the central coast of the western Bohai Sea, although a significant levering effect was identified in the early Holocene, strong local signals (e.g., delta sediment loading and groundwater extraction) affected the results soon after the ESL rise slowed down, hindering recognition of the mid-Holocene sea-level highstand (e.g., Wang et al., 2020, 2024).

During the Holocene, the southern Bohai Sea coast, located hundreds of kilometers east from the Holocene Yellow River mega-delta system, developed primarily on a small, proximal sandy delta. Moreover, this area is generally regarded as geologically stable (Liu et al., 2022), and has experienced only limited modern land subsidence due to groundwater extraction (Su et al., 2021; Liu et al., 2022). Consequently, it could be an ideal location for paleo-sea-level reconstruction to test the far-field mid-Holocene highstand and to understand the associated GIA processes.

## 2. Regional setting

The Bohai Sea, positioned in the innermost part of the East Asian marginal seas, is characterized by an extensive continental shelf extending up to 1500 km from the Japan Trenches. On its east side, the Shandong Peninsula and the Liaodong-Korean Peninsula form a pathway linking the semi-enclosed Bohai Sea to the Yellow Sea and the East China Sea (Fig. 1a). During the LGM, the Bohai Sea region was fully exposed and suited about 1000 km away from the coastal line at Asia outer shelf (Qin et al., 1990). Under the context of deglacial sea-level rise, the seawater intrusion occurred around the North Yellow Sea to Bohai Strait at the beginning of the Holocene (Liu et al., 2004, 2007). Following the early Holocene transgression, the coastline of Bohai Bay retreated tens of kilometers inland, reached the marine transgression limit at 6000–7000 cal a BP, and gradually prograded seaward along with the rivers supplied large amounts of sediment to the coast (Qin et al., 1990; Xue, 1993; Xue and Ding, 2008; Tian et al., 2011, 2017; Wang et al., 2015). The Yellow River formed a mega-delta system with nine superlobes along the central coast western Bohai Sea during the Holocene (Xue, 1993). However, for much of this period, the southern Bohai Sea coast was distant from the paleo-Yellow River deltas. Even when the river discharged relatively closer in the late Holocene, such as during 11–1048 CE and after 1855 CE, it remained over 100 km from the study area, likely contributing only limited sediment. As a result, the southern coast developed a small, proximal sandy delta with deposits less than 10 m thick, extending approximately 20 km (Xue and Ding, 2008).

The southern Bohai Sea features the semicircular Laizhou Bay, opening northward and located between the Shandong Peninsula to the east and the modern Yellow River Delta to the west (Fig. 1b). Water depths in this bay are generally less than 10 m. In Laizhou Bay, the mean

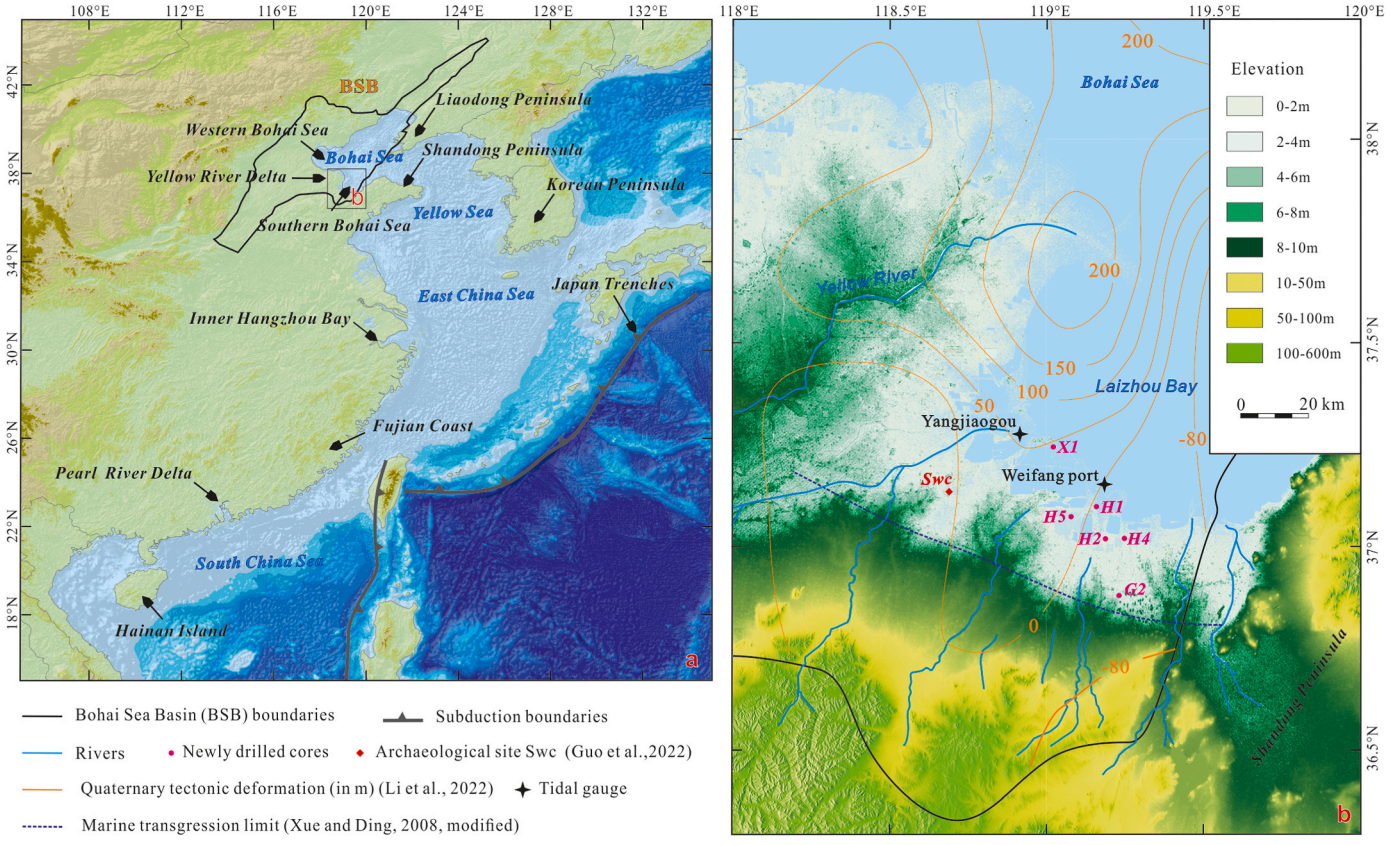


**Fig. 1.** (a) An overview map of East Asia showing the geological site of the Cenozoic Bohai Sea Basin (BSB) and the locations of the southern Bohai Sea coast, with other locations discussed in this paper; (b) a detailed landscape of the southern Bohai Sea coast with Holocene marine transgression limit, Quaternary tectonic deformation, tidal gauges, cores locations (G2, H1, H2, H4, H5, and X1) and archaeological site (Swc).

spring tidal range (MSTR) is 1.62 m (Zhang and Wang, 1999); the mean tidal range (MTR) and the mean neap tidal range (MNTR) are 0.75 m and 0.50 m, respectively (Sun et al., 2018).

From a basin perspective, the study area lies within the Bohai Sea Basin (BSB) (Fig. 1a), the largest Cenozoic rift basin in eastern China, resulting from mantle dynamics associated with the subduction of the western Pacific plate during the Cenozoic era (Allen et al., 1997). This basin experienced rapid tectonic subsidence during the Cenozoic, typically with the accumulation of lacustrine and fluvial sediments up to several kilometers thick (Allen et al., 1997; Hu et al., 2001; Huang et al., 2014). It transformed into an inner shelf sea hundreds of thousands of years ago (Huang et al., 2014; Yi et al., 2016). Situated approximately 1500 km from active subduction zones, the southern Bohai Sea coast exhibits low seismicity, with several recorded M6+ earthquakes over the past 400–500 years concentrated roughly 200 km north in the central Bohai Sea or 100 km south near the mountain-basin boundaries (cf. Liu et al., 2022). These earthquakes were mainly controlled by strike-slip faults which were predominantly extensional or transtensional within Quaternary strata (Xu et al., 2019). Limited seismic and faulting activity along the southern Bohai Sea coast contributed to its geological stability (cf. Huang et al., 2014; Liu et al., 2022). Liu et al. (2022) quantified the anomalous subsidence of the BSB by removing earlier thermal subsidence from observed tectonic subsidence and suggested Quaternary vertical deformation along the southern Bohai Sea coast ranges between −80 and 50 m (with positive values indicating subsidence) (Fig. 1b).

Since the 1950s, especially after the 1970s, extensive groundwater extraction has led to severe land subsidence in the North China Plain. Based on precise leveling data, Su et al. (2021) detailed the cumulative modern subsidence with spatial extent and accuracy, highlighting that severely subsiding regions have developed mainly along the surrounding coasts of western Bohai Sea, with total subsidence ranging broadly from 0.6 to 2.6 m, only slight subsidence has been observed along the southern Bohai Sea coast, ranging from 0 to 20 cm.

## 3. Material and methods

### 3.1. Cores and sample elevations

Sedimentary samples chosen for this study are from six new cores (G2, H1, H2, H4, H5, and X1) and one previous archaeological study of Shuang Wang Cheng (Swc) (Guo et al., 2022) (Fig. 1b–Table 1). Elevations for all sites were tied to the mean sea level (MSL) of the National Yellow Sea 85 Datum. Elevations for the six new cores were leveled using the GPS-RTK system by the CORS network with an uncertainty of 2 cm. All cores were rotary drilled with depth errors estimated at 5 cm. The archaeological site Swc, located on a flat coastal plain, was excavated down to a depth of 2.5m with negligible depth error, and its elevation was determined to be 3.5 m MSL with an uncertainty of 0.5 m, based on a local bathymetric map with a 1 m contour interval (Guo et al., 2022). In newly drilled cores, dated macrofossil samples, such as various mollusks or peat fragments, were logged with a vertical uncertainty of 1 cm. At the archaeological site Swc, however, the dated foraminifera were extracted from 5 cm thick sediment layers (Guo et al., 2022).

Pleistocene base depth values, identified via sedimentary method (section 4.1), can be used as incompressible positions to calculate the compaction loss for samples in strata (section part 3.6). For archaeological site Swc (Guo et al., 2022), due to a lack of deeper strata information, the maximum Pleistocene basement depth was set the same as core H2 to account for all possible contributions (see Fig. 3 for core correlation). The quantified Quaternary tectonic deformation was from Liu et al. (2022).

### 3.2. Radiocarbon dating and calibration

Dating materials were selected from sedimentary archive levels containing macrofossils that could provide reliable ages for the Holocene stratigraphic framework, particularly within transgressive and regressive sequences, to generate sea-level index points (SLIPs). For organic-rich sediments, extracted terrestrial macrofossils (in this study, plant fragments and gastropod *Bithynia fuchsiana*) served as ideal dating materials, providing more accurate ages than bulk peat samples (e.g., Törnqvist et al., 1992). For marine sediments, in the absence of in vivo doublets, intact marine mollusk with thin shells (e.g., *Potamocorbula laevis* and *Assiminea latericea*), or those with vivid surface coloration (such as *Umbonium thomasi*, *Neverita didyma*, *Dosinia biscocta*, *Dosinia japonica*, and *Meretrix meretri*) were selected as substitutes to help reduce potential reworking durations. Based on these materials, we obtained 19 accelerator mass spectrometry (AMS) $^{14}$C ages from newly drilled cores, reported by the School of Archaeology and Museology at Peking University. Two dated foraminifera AMS $^{14}$C ages from a previous archaeological site Swc were also included (Table 2). All conventional ages were calibrated to calendar years relative to 1950 CE using the latest version of Calib 8.20 (Reimer et al., 2020), with the Intcal20 curve for freshwater samples (plant fragments and gastropod) or the Marine20 curve (Heaton et al., 2020) for marine mollusk samples, applying a ΔR value of −334 ± 50 from marine shell samples in the Bohai Sea (Southon et al., 2002).

### 3.3. Tidal datums

SLIPs are typically defined relative to a tidal datum. However, the heights of these datums have varied throughout the Holocene in response to sea-level change and related change in coastal configuration and water depth (Hijma and Cohen, 2019). During the early Holocene, with sea levels steadily rising but significantly lower than today, numerical simulations suggest a tidal-influenced marine environment with an expanded semi-enclosed bay extending from the East China Sea and the Yellow Sea into the Bohai Sea (Uehara and Saito, 2003; Chen and Zhu, 2012). Chen and Zhu (2012) indicate that after ~10,000 cal a BP, as seawater entered the Bohai Sea region, tidal currents became weak, with a further marked decrease during the Holocene maximum transgression. This trend is supported by sedimentary evidence from Yao et al. (2017), noting a drop in tidal currents around 6700 cal a BP in the eastern Bohai Sea. By ~6000–7000 cal a BP, tidal patterns became generally consistent with those observed today (Zhu and Chang, 2000; Chen and Zhu, 2012; Yao et al., 2017). Theoretically, relatively strong

**Table 1**
Cores information for this study.

| Core | Position | | Elevation/m | Pleistocene base/m | Land subsidence/m (in 1960–2010s) | Quaternary Tectonic deformation | |
|---|---|---|---|---|---|---|---|
| | Lat. | Lon. | | | | Total deformation/m | Average rate/m kyr$^{-1}$ |
| G2 | 36.901 | 119.149 | 6.30 | 3.0 | 0.1 ± 0.1 | −40 ± 40 | −0.02 ± 0.02 |
| H2 | 37.033 | 119.138 | 3.45 | 8.4 | 0.1 ± 0.1 | −40 ± 40 | −0.02 ± 0.02 |
| H4 | 37.031 | 119.189 | 3.57 | 10.3 | 0.1 ± 0.1 | −40 ± 40 | −0.02 ± 0.02 |
| H5 | 37.094 | 119.041 | 3.54 | 10.6 | 0.1 ± 0.1 | 25 ± 25 | 0.01 ± 0.01 |
| H1 | 37.107 | 119.119 | 2.35 | 11.0 | 0.1 ± 0.1 | 0 ± 25 | 0 ± 0.01 |
| X1 | 37.253 | 119.018 | 0.88 | 17.0 | 0.1 ± 0.1 | 50 ± 25 | 0.02 ± 0.01 |
| Swc | 37.107 | 119.119 | 3.50 | 8.4 | 0.1 ± 0.1 | 0 ± 25 | 0 ± 0.01 |

**Table 2**
Ages on cores G2, H1, H2, H4, H5, X1 as well as archaeological site Swc for this study.

| Sample ID | Depth/m | Dated material | Conventional $^{14}$C age/a BP | Calib curve | Calibrated age (cal yr BP) | | | | | Lab. no. |
|---|---|---|---|---|---|---|---|---|---|---|
| | | | | | Median | 1 σ | Prob. | 2 σ | Prob. | |
| G2-1 | 2.63 | *Bithynia fuchsiana* | 6180 ± 30 | Intcal20 | 7073 | 7015–7126 | 0.965 | 6979–7165 | 0.998 | BA140745 |
| H2-1 | 2.16 | *Umbonium thomasi* | 4945 ± 30 | Marine20 | 5451 | 5358–5546 | 1 | 5273–5621 | 1 | BA121364 |
| H2-2 | 5.51 | *Potamocorbula laevis* | 5280 ± 35 | Marine20 | 5803 | 5710–5902 | 1 | 5601–5986 | 1 | BA121365 |
| H2-3 | 6.82 | *Dosinia biscocta* | 5740 ± 35 | Marine20 | 6306 | 6211–6391 | 1 | 6112–6494 | 1 | BA121366 |
| H2-4 | 7.21 | *Meretrix meretrix* | 6940 ± 30 | Marine20 | 7560 | 7481–7640 | 1 | 7406–7726 | 1 | BA121367 |
| H4-1 | 2.75 | *Potamocorbula laevis* | 4750 ± 20 | Marine20 | 5230 | 5109–5327 | 1 | 5015–5441 | 1 | BA140327 |
| H4-2 | 6.53 | *Meretrix meretrix* | 5960 ± 50 | Marine20 | 6537 | 6429–6644 | 1 | 6317–6743 | 1 | BA140330 |
| H4-3 | 8.20 | *Potamocorbula laevis* | 6235 ± 40 | Marine20 | 6851 | 6739–6952 | 1 | 6639–7074 | 1 | BA140332 |
| H5-1 | 3.15 | *Potamocorbula laevis* | 4175 ± 30 | Marine20 | 4506 | 4396–4616 | 1 | 4289–4736 | 0.992 | BA140749 |
| H5-2 | 4.85 | *Dosinia Japonica* | 4610 ± 25 | Marine20 | 5057 | 4943–5184 | 1 | 4851–5268 | 1 | BA140751 |
| H5-3 | 8.34 | *Assiminea lutea* | 7450 ± 30 | Marine20 | 8068 | 7982–8155 | 1 | 7902–8267 | 1 | BA140753 |
| H1-1 | 2.55 | *Umbonium thomasi* | 2955 ± 30 | Marine20 | 2947 | 2842–3050 | 1 | 2755–3148 | 1 | BA121359 |
| H1-2 | 3.45 | *Meretrix meretrix* | 3160 ± 25 | Marine20 | 3208 | 3118–3319 | 1 | 2998–3388 | 1 | BA121360 |
| H1-3 | 5.53 | *Neverita didyma* | 4800 ± 30 | Marine20 | 5297 | 5209–5425 | 1 | 5052–5483 | 1 | BA121361 |
| X1-1 | 4.11 | *Potamocorbula laevis* | 1735 ± 20 | Marine20 | 1467 | 1373–1546 | 1 | 1297–1642 | 1 | BA140322 |
| X1-2 | 10.15 | *Potamocorbula laevis* | 7320 ± 25 | Marine20 | 7930 | 7844–8011 | 1 | 7754–8118 | 1 | BA140323 |
| X1-3 | 11.15 | *Potamocorbula laevis* | 2000 ± 20 | Marine20 | 1779 | 1689–1875 | 1 | 1592–1971 | 1 | BA140324 |
| X1-4 | 12.32 | plant fragment | 7650 ± 25 | Intcal20 | 8426 | 8400–8450 | 1 | 8383–8483 | 0.900 | BA140325 |
| X1-5 | 16.38 | plant fragment | 8060 ± 30 | Intcal20 | 8994 | 8810–9021 | 0.990 | 8778–9027 | 0.959 | BA140326 |
| Swc-1 | 1.08 | foraminifera | 5135 ± 60 | Marine20 | 5655 | 5543–5765 | 1 | 5452–5882 | 1 | BA10366 |
| Swc-2 | 2.36 | foraminifera | 5945 ± 35 | Marine20 | 6405 | 6421–6622 | 1 | 6321–6716 | 1 | BA10367 |

tidal currents in the early Holocene would have increased tidal amplitudes centered on the paleo-head of the Bohai Sea (further inland from the western Bohai Sea coast), a region even farther from the study area than today. Thus, any variability in tidal amplitude throughout the Holocene was likely limited, making present-day average multi-year tidal statistics (Table 3) suitable as reference levels for SLIPs.

Mean Higher High Water (MHHW) and Mean Lower Low Water (MLLW) are based on the Yangjiaogou gauge's 23-year observations (Zhang and Wang, 1999). The highest tidal record of 3.34 m MSL in 1992 (Zhang and Wang, 1999) served as the Highest High Water (HHW) in this study. Mean High Water (MHW), Mean Low Water (MLW), Mean High Water Neaps (MHWN), and Mean Low Water Neaps (MLWN) are deduced using a 3-year statistics from the Weifang port tide gauge (Sun et al., 2018).

### 3.4. Sedimentary identifications and sea-level indicative meanings

In the laboratory, the sediment cores were opened, photographed, and recorded for sedimentary characteristics, including grain size, Munsell color, physical sedimentary structures, organics, macrofossils, and bioturbations. To help determine the sedimentary environments, samples were taken for grain-size and foraminifera analysis.

The grain-size samples were pretreated with 10–20 ml of 30% $H_2O_2$ to remove organic matter, and then with 10% HCl to remove biogenic carbonates. They were rinsed with deionized water and placed in an ultrasonic vibrator for several minutes to facilitate dispersion. Fifty grain-size classes between 0.2 and 2000 μm were determined using a Microtrac S3500 Particle Size Analyzer.

Foraminifera larger than 154 μm were floated with carbon tetrachloride, which has a specific gravity of 1.59, for quantitative analysis. Foraminifera analysis involved considerations of abundance and assemblage characteristics. For coastal foraminifera zonation, we referred to studies from the western Bohai Sea, which indicated that foraminifera on supratidal flats are sparse and dominated by brackish/euryhaline species, those on upper flats range from few to abundant and are dominated by euryhaline species, while those on mid-lower flats and subtidal marine areas are abundant and dominated by marine/euryhaline species (Li et al., 2010, 2016). Notably, the foraminifera species *E. simplex* was found to concentrate above tidal flats (about >1%) and thrive within upper flats (3–67%) (Li et al., 2010, 2016), making it an effective tidal flat (especially upper flat) reference.

Dated supratidal, upper-tidal, and mid-lower tidal flat sediments were used to develop SLIPs. Regarding the indicative meanings of each sedimentary type, we followed the definition provided in the *Handbook of Sea-level Research* Chapter 33 (Vis et al., 2015). Supratidal flat deposits are located above the highest regular tidal inundation (MHHW to HHW). The upper flat is briefly inundated during regularly occurring higher tides (MHWN to MHHW). The middle and lower flats experience more frequent inundation during most tidal periods (MLLW to MHWN) and are challenging to further subdivide due to their environmental similarity; hence, we combined them into a single category as mid-lower flat. To contribute to the database of global RSL dataset, we followed the guidelines of Khan et al. (2019) and documented the indicative meaning for this study in Table 4, including sample type, supporting evidence, and algebraic expression with reference water level and indicative range. See section 4.1 for sample type identification.

### 3.5. Correction of tectonic effects, water extraction effects, and sediment compaction effects

Using Quaternary vertical deformation values (ranging from −40 to 50 m, with errors of 40 or 25 m) for each core site (cf. Liu et al., 2022), divided by 2.58 Ma, we calculated average tectonic deformation rates to adjust the SLIPs in this study (Table 1).

Since the 1950s, only slight land subsidence has been observed along the southern Bohai Sea coast, ranging from 0 to 20 cm (cf. Su et al., 2021). Therefore, we compensated for the elevation of each sample site by adding 0.1 ± 0.1 m of leveling.

The estuarine sequence is estimated to undergo linear increasing compaction after deposition, with up to a 10% loss rate for early

**Table 3**
Reference tidal levels for study area (m, elevation, MSL).

| Location | HHW | MHHW | MHW | MHWN | MLWN | MLW | MLLW | Data source |
|---|---|---|---|---|---|---|---|---|
| Yangjiaogou | 3.34 | 0.73 | | | | | −0.88 | 1972–1994 (Zhang and Wang, 1999) |
| Weifang port | | | 0.38 | 0.25 | −0.25 | −0.38 | | 2013–2015 (Sun et al., 2018) |

**Table 4**
Environment identifications and their indicative meanings (m, elevation, MSL).

| Type | Evidence | | Reference water level | Indicative range | Indicative meaning |
|---|---|---|---|---|---|
| | Foraminifera characteristics | Sedimentary characteristics | | | |
| Supratidal flat | low abundance (0–$10^2$/g), brackish/euryhaline species dominated, *E. simplex*: >1% | sandy silt; organics; lack of marine mollusk; few terrestrial gastropods. | (MHHW + HHW)/2 | HHW – MHHW | 2.04 ± 1.31 |
| Upper flat | low abundance (0–$10^2$/g), euryhaline species dominated, *E. simplex*: >3% | sandy silt; organics; Fe oxides; occasional bioturbations and marine mollusk. | (MHWN + MHHW)/2 | MHHW – MHWN | 0.49 ± 0.24 |
| Mid-lower flat | high abundant ($10^2$–$10^3$/g), marine/euryhaline species dominated, *E. simplex*: >1% | silty sand; flaser bedding; common presence of marine mollusk. | (MLLW + MHWN)/2 | MHWN – MLLW | −0.32 ± 0.57 |

Holocene coastal sediments (Xiong et al., 2018, 2020). To correct sediment compaction for intercalated SLIPs, we followed this approach and calculated the total amount lowering as 10% of the initial thickness of compressible layers beneath the dated horizon divided by the post-depositional lapse time proportional to the past 9000 years. The Pleistocene fluvial basement (for depth listed in Table 1), identified via sedimentary methods (see section 4.1), serves as the incompressible position to calculate the compaction loss for samples in strata.

### 3.6. Sea-level trends analyses

As described above, SLIPs can be further corrected for post-depositional changes in elevations by accounting for all lowering effects due to water extraction, tectonic subsidence, and coastal strata self-compaction. The vertical uncertainty is calculated by taking the square root of the quadratic sum of all individual sources of uncertainty (e.g. Hijma et al., 2015). An integrated Gaussian process EIV-IGP model of Cahill et al. (2015, 2016) was employed to estimate the non-linear trend underlying the noisy sea-level data and to generate a sea-level curve with 1σ and 2σ probabilistic intervals.

## 4. Results

### 4.1. Stratigraphic framework and sedimentary facies identification

The sediment records from different sites (G2, Swc, H1, H2, H4, H5, and X1; see positions in Fig. 1b) form a hypothetical seaward transect based on their distances from the marine transgression limit and the present coastline (Fig. 2). Sedimentary facies were examined through a combination of foraminifera tests and sedimentary analysis (Fig. 3). The Holocene strata in all cores are underlain by brown, stiff sandy sediments featuring calcareous nodules and leaching of Fe oxide. Regionally, these sediments were interpreted as the Pleistocene basement, which originated from fluvial deposits and underwent subsequent pedogenic processes during the LGM (Qin et al., 1990). The Pleistocene basement, positioned at a depth of 3.0 m (3.30 m in elevation) in core G2, decreases gradually southward, reaching a depth of 17.0m (−16.12m in elevation) in core X1 (Fig. 2).

Above the Pleistocene basement, the Holocene marine-related archives reveal a transgressive-regressive sequence. The Holocene stratigraphic framework and the sedimentary facies identification are provided as follows.

#### 4.1.1. Sedimentation during marine transgression

In cores G2, H2, H4, H5, H1, and X1 (Fig. 3), the basal sediments above the Pleistocene basement were generally composed of a few meters of yellowish-grey or dark greyish silts with varying amounts of organic vegetation, occasional Fe oxides, and some interbedded sand layers (as seen in core X1). Foraminifera were rarely preserved (abundance <5/g) in the basal sediments of cores H2, H4, H5, H1, and X1, predominantly consisting of euryhaline species such as *A. beccarii* vars. and/or *E. magellanicum*. In contrast, the foraminifera in core G2 ranged from rare to abundant (abundance 1–85/g) and showed a high proportion of brackish species (25–50%) such as *P. variabilis* and *P. sinensis*, along with significant presence of euryhaline species (28–37%) and various marine species (22–38%). In all cores, the proportion of *E. simplex* ranged from 3 to 15% in the basal sediments. Despite the lack of marine shells, terrestrial gastropods such as *Bithynia fuchsiana* and *Gyraulus albus*, along with related opercula, were identified from this unit. These basal sediments were interpreted as being deposited in a coastal fluvial environment influenced by coastal river flooding and sea storms, characteristic of a supratidal flat. Within this basal unit, two dated peat plants in core X1 yielded 2 σ age ranges of 8383–8483and 8778–9027cal a BP, while a dated terrestrial gastropod in core G2 yielded a 2 σ age range of 6979–7165 cal a BP.

In cores H2 and H5 (Fig. 3), above the basal supratidal flat sediments, brown or olive grey sandy silts with few Fe oxides, bioturbations, or organics were found, separated from the underlying sediments by sharp contacts. Few marine mollusks, such as the upper tidal marine mollusk *Assiminea latericea* and the tidal-subtidal marine mollusk *Meretrix*

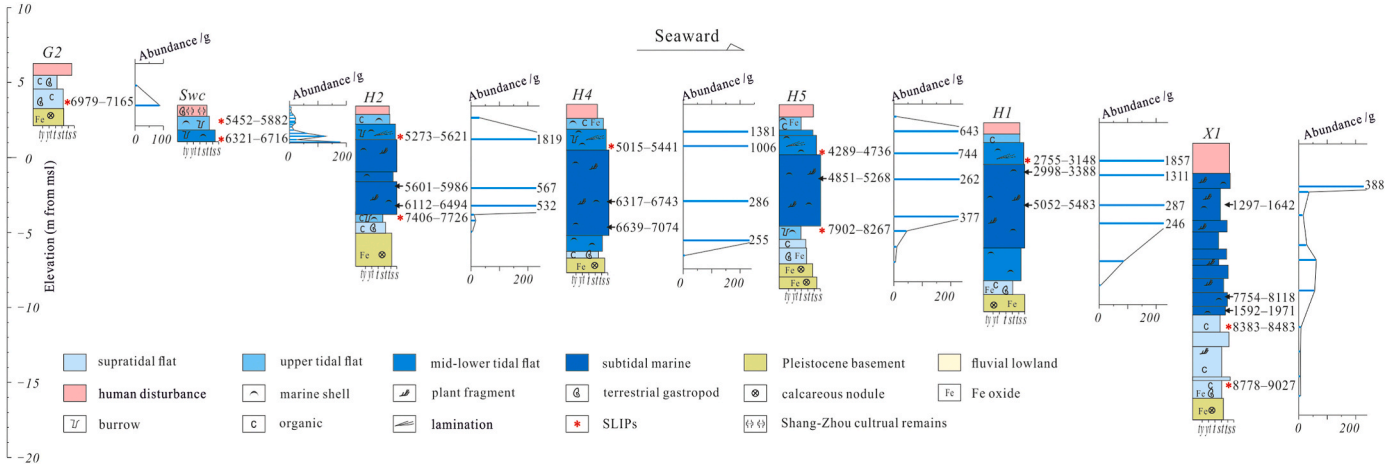


**Fig. 2.** A sedimentological transect with foraminiferal abundance curves depicting a marine-related sequence along the southern Bohai Sea coast.

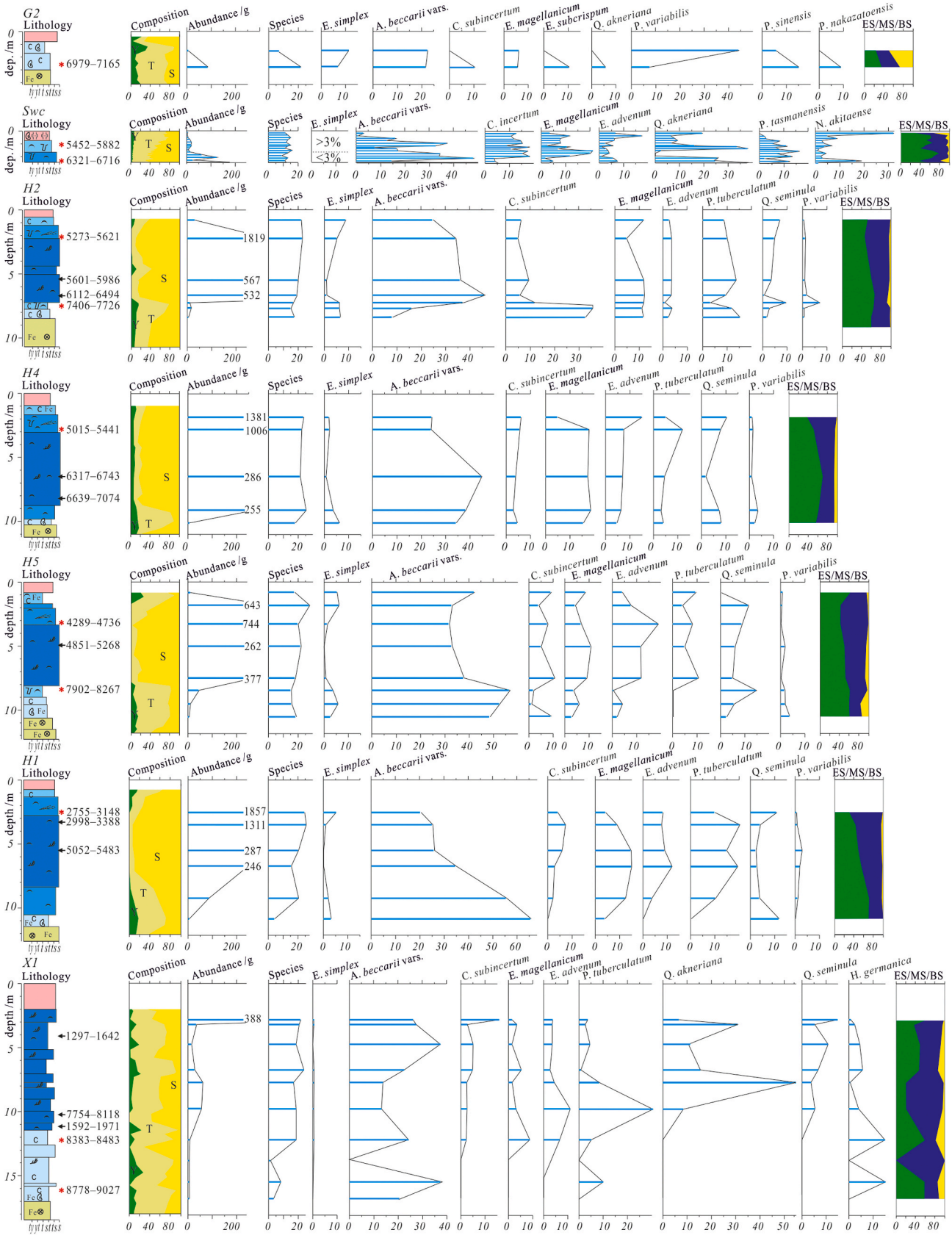


**Fig. 3.** Detailed profiles with lithology, sedimentary environment, AMS $^{14}$C age, sediment composition, and foraminifera data. Y, clay; T, silt; S, sand; ES, euryhaline species; MS, marine species; BS, brackish species. Legend for column sedimentary features same as in Fig. 2.

*meretrix*, were occasionally present. The foraminifera in this unit were few (abundance 10–50/g), predominantly comprising euryhaline species (60–70%), especially dominated by *A. beccarii* vars. Various marine species constituted the second largest proportion (30–35%), while the proportion of brackish species remained relatively low (normally 5–10%). Notably, the presence of *E. simplex* was consistently above 6% (6–14%). These sediments were interpreted as being deposited under conditions of shorter tidal submersion and longer tidal exposure, characteristic of an upper tidal flat environment. Two $^{14}$C ages of marine mollusks were obtained from these upper tidal flat sediments in cores H5 and H2, with 2 σ age ranges of 7902–8267 and 7406–7726 cal a BP.

While in cores H4 and H1 (Fig. 3), above the basal supratidal flat sediments with sharp contacts, grayish-brown silty sands were found instead. The sediment structure was unclear due to drilling disturbances, but tidal-subtidal species such as *Potanocorbula laevis* and *Meretrix meretrix* were found. The foraminifera in this unit were present to abundant (82–255/g), primarily dominated by euryhaline species (55–71%), such as *A. beccarii* vars. and various marine species (27–39%). Brackish species consistently made up 2–6%, while *E. simplex* was observed at levels above 1–3%. This unit was interpreted as having been deposited under conditions of longer tidal submersion, characteristic of a mid-lower tidal flat. No age dating was available for this unit.

#### 4.1.2. Sedimentation during marine inundation

In cores H2, H4, H5, and H1 (Fig. 3), the sediments above the transgressive upper or mid-lower tidal flat sediments are grayish bulk sorted sands containing scattered various marine mollusks, including typical subtidal species such as bivalves *Mactra veneriformis, Dosinia biscocta*, *Dosinia japonica* and gastropods *Neverita didyma*, *Terebra bellanodosa*. Foraminifera were highly abundant (250–600/g), predominantly consisting of euryhaline species (43–70%) and marine species (25–45%), with *E. simplex* constituting less than 1% and brackish species less than 5%. These sediments were interpreted as having been deposited in submerged conditions of a subtidal marine environment. Within this unit, seven $^{14}$C dates of marine mollusks from cores H4, H2, H5, and H1 yielded 2 σ ages of 6639–7074, 6317–6743, 6112–6494, 5601–5986, 4851–5268, 5052–5483, and 2998–3388cal a BP.

In core X1 (Fig. 3), located at the most seaward position in the study area, the sediments above the transgressive unit (from a depth of 2.2–11.0 m) were composed of grayish sandy silt with some yellowish sandy interlayers. Marine mollusks were rare and only *Potanocorbula laevis* to be observed, and foraminifera were found in low abundance (13–60/g). The proportions of euryhaline, marine, and brackish species varied significantly. Three marine mollusks $^{14}$C dates were obtained with 2 σ age ranges of 1592–1971, 7754–8118, and 1297–1642 cal a BP, respectively. These sediments were interpreted as having been rapidly deposited within a subaqueous channel during ~1800–1500 cal a BP, with the 7754–8118 cal a BP age likely representing reworked material from upstream. Nevertheless, these subaqueous channel deposits are labeled under the general term of subtidal marine in the core.

#### 4.1.3. Sedimentation during marine regression

In site Swc and cores H2, H4, H5, and H1 (Fig. 3), the sediments at shallow depth transitioned into grayish-brown or olive-brown silty sand which included a few flaser laminations and bioturbations. Gradual contacts were observed in cores H2, H4, H5, and H1 with the underlying sorted subtidal sand. Commonly observed tidal marine mollusks included *Sinonovacula constricta*, *Umbonium thomasi*, *Moerella jedoensis*, and tidal-subtidal marine mollusks such as *Meretrix meretrix* and *Potanocorbula laevis*. The foraminifera in this unit were very abundant (100–1000/g), primarily dominated by various marine species (45–70%) and euryhaline species (30–50%) such as *A. beccarii* vars., Brackish species consistently made up a minority (normally <5%), while *E. simplex* was observed at levels above 1% but less than 6%. This unit was interpreted as having been deposited under conditions of longer tidal submersion, characteristic of a mid-lower tidal flat. Four marine mollusks from this unit in cores H2, H4, H5, and H1 provided 2 σ age ranges of 5273–5621, 5015–5441, 4289–4736, and 2755–3148 cal a BP, respectively. A dated foraminifera sample from site Swc yielded a 2 σ age of 6321–6716 cal a BP (Guo et al., 2022).

There is a consistent increase in silt content above the underlying mid-lower tidal flat unit. These sediments are characterized by their yellowish grey or pale brown color, sandy silt composition, weak presence of iron oxides, occasional bioturbations and marine mollusks. The foraminifera present in this unit are sparse (10–30/g), predominantly euryhaline species (60–70%) with *A. beccarii* vars., being particularly common. Marine species make up the second largest proportion (30–35%), while brackish species are relatively low (5–10%), with *E. simplex* identified at levels above 6% (6–14%). Upper tidal marine mollusks species such as *Cerithidea sinensis* and *Assiminea latericea* were found at site Swc and in core H2. A dated foraminifera sample from this unit at site Swc yielded a 2 σ age range of 5452–5882 cal a BP (Guo et al., 2022).

#### 4.1.4. Human disturbance and archaeological findings

The study cores were drilled in farmland or industrial areas, where the ground sediments were affected to varying degrees by human disturbance, typically down to depths of 0.5–1.0 m. Due to this, these disturbed upper sediments were deemed unreliable for reconstructing past sea levels.

However, the analysis from the archaeological site Swc revealed that the sediments at depths of 0–0.7 m consisted of grayish sandy silt containing some archaeological remains (Fig. 3). Despite the human historical disturbance, this unit still contained rare foraminifera (with an abundance of 1–4/g), predominantly *C. incertum* and *Q. akneriana*. *E. advenum*. Additionally, a terrestrial gastropod, *Pseudamnicola opima*, was found at a depth of approximately 0.4 m. The archaeological remains included helmet-shaped pottery and associated brine wells from the Shang-Zhou period (approximately 3.5–2.2 BP) (Guo et al., 2022).

### 4.2. Sea-level index points and RSL changes

After sedimentary facies identification, a total of 11 SLIPs were established from the $^{14}$C-dated supratidal, upper-tidal, and mid-lower tidal flat sediments. These SLIPs were further corrected for possible sedimentary self-compaction, long-term tectonic effect, and the lowering effect due to water extraction. Core information and detailed radiocarbon dating and calibration are listed in Tables 2 and 3 For each SLIP, evidence for sedimentary facies, correction for post-depositional lowering, and the indicative meanings are compiled in Table 5.

Based on these SLIPs, the RSL changes over an age range of 9000–3000 cal a BP are reconstructed as shown in Fig. 4. Five SLIPs older than 7000 cal a BP (ID. X1-5, X1-4, H5-3, H2-4, and G2-1, Tables 3 and 5) were all formed during the marine transgression (Fig. 4), while other six younger than 7000 cal a BP SLIPs (ID. Swc-2, Swc-1, H1-1, H5-1, H4-1, and H2-1, Tables 3 and 5) were generated during marine regression (Fig. 4).

The five oldest SLIPs (ID. X1-5, X1-4, H5-3, H2-4, and G2-1, Tables 3 and 5) indicate a period of rapid RSL rise from about $-17.19 \pm 1.32$ m to $1.62 \pm 1.32$ m MSL between 9000 and 7000 cal a BP. During this 2000-year span, the reconstructed RSL changes by the EIV-IGP model show that the rates of RSL rise were very high during 9000 to 8000cal a BP, around 8–10 mm/a. After 8000 cal a BP, the rate decreased rapidly to ~4 mm/a by 7000 cal a BP (Fig. 4). Interestingly, RSL continued to rise after 7000 cal a BP: a set of mid-Holocene SLIPs (ID. G2-1, Swc-2, Swc-1, H5-1, H4-1, and H2-1, Table 5) provides compelling evidence for a higher-than-present mid-Holocene highstand (Fig. 4). The modeled RSL rose after 7000 cal a BP with the rate gradually decelerating to 0 mm/a, reaching its highest highstand of $2.44 \pm 1.34$ m MSL by approximately 6000 cal a BP. Following this peak, there was a clear trend of RSL fall, with a maximum falling rate of 1.2 mm/a around 5000 cal a BP. The sea level reached its present height after 3000–4000 cal a BP, supported by

**Table 5**
SLIPs from cores G2, H1, H2, H4, H5, and X1 and previous works from Swc on the southern Bohai Sea coast.

| ID | Cal. (2σ) date /cal a BP | depth/m | Depth to consolidated substrate /m | Sample elevation & error /m, MSL | Sample type | Supporting evidence | | | | | | | Sample indicative meaning | Indicative meaning /m, MSL | RSL & range /m | Post-depositional correction for sample elevation | | | Corrected RSL & range /m, MSL |
|---|---|---|---|---|---|---|---|---|---|---|---|---|---|---|---|---|---|---|---|
| | | | | | | Features and macrofossils | Foraminifera | | | | | | | | | Compac. /m | Tectonic deformation & error/m | Ground lowering & error/m | |
| | | | | | | | Abun./g | Assemb. | Es % | B % | E % | M % | Sp. | | | | | | |
| G2-1 | 6979–7165 | 2.63 | 0.37 | 3.67 ± 0.05 | Supra tidal flat | 2.5Y 4/2 dark greyish brown, sandy silt, organic, terrestrial gastropod: Bf and opercula | 85 | Ab, Ps, Cs, Pn | 7 | 25 | 37 | 38 | 23 | HHW – MHHW | 2.04 ± 1.31 | 1.63 ± 1.31 | 0.03 | −0.14 ± 0.14 | 0.1 ± 0.1 | 1.62 ± 1.32 |
| H2-1 | 5273–5621 | 2.16 | 6.24 | 1.29 ± 0.05 | Mid-lower tidal flat | 2.5 YR 5/4 light olive brown, silty sand, burrows, flaser laminations, tidal marine mollusk: Ut | 1819 | Ab, Pt, Qs, Em, Cs | 3 | 4 | 46 | 50 | 23 | MHWN – MLLW | −0.32 ± 0.57 | 1.61 ± 0.57 | 0.40 | −0.10 ± 0.10 | 0.1 ± 0.1 | 2.00 ± 0.59 |
| H2-4 | 7406–7726 | 7.21 | 1.19 | −3.76 ± 0.05 | Upper tidal flat | 10 YR 4/2 dark greyish brown, sandy silt, organic, tidal-subtidal marine mollusk: Mm | 13 | Cs, Ab, Em | 6 | 1 | 64 | 35 | 16 | MHHW – MHWN | 0.49 ± 0.24 | −4.25 ± 0.25 | 0.11 | 0.16 ± 0.16 | 0.1 ± 0.1 | −4.19 ± 0.31 |
| H4-1 | 5015–5441 | 2.75 | 7.55 | 0.82 ± 0.05 | Mid-lower tidal flat | 10 YR 4/2 dark greyish brown, silty sand, flaser laminations, burrows, tidal-subtidal marine mollusk: Pl | 1006 | Ab, Em, Pt, Qs | 2 | 5 | 51 | 44 | 22 | MHWN – MLLW | −0.32 ± 0.57 | 1.14 ± 0.57 | 0.47 | −0.10 ± 0.10 | 0.1 ± 0.1 | 1.61 ± 0.59 |
| H5-1 | 4289–4736 | 3.15 | 7.45 | 0.39 ± 0.05 | Mid-lower tidal flat | 10 YR 4/3 brown, silty sand, flaser laminations, marine mollusk: Pl | 744 | Ab, Ea, Qs, Pt | 1 | 1 | 41 | 58 | 19 | MHWN – MLLW | −0.32 ± 0.57 | 0.71 ± 0.57 | 0.39 | 0.05 ± 0.05 | 0.1 ± 0.1 | 1.25 ± 0.58 |
| H5-3 | 7902–8267 | 8.34 | 2.26 | −4.80 ± 0.05 | Upper tidal flat | 10 YR 4/2 dark greyish brown, sandy silt, burrows, organic, tidal marine mollusk: Al | 45 | Ab, Ea, Pt, Em | 3 | 3 | 61 | 36 | 17 | MHHW – MHWN | 0.49 ± 0.24 | −5.29 ± 0.25 | 0.22 | 0.08 ± 0.08 | 0.1 ± 0.1 | −4.89 ± 0.28 |
| H1-1 | 2755–3148 | 2.55 | 8.45 | −0.20 ± 0.05 | Mid-lower tidal flat | 2.5 YR 5/4 light olive brown, silty sand, flaser laminations, tidal marine mollusk: Ut | 1857 | Ab, Qs, Pt, Tt | 5 | 1 | 30 | 69 | 24 | MHWN – MLLW | −0.32 ± 0.57 | 0.12 ± 0.57 | 0.29 | 0 ± 0.03 | 0.1 ± 0.1 | 0.51 ± 0.58 |

(*continued on next page*)

**Table 5** (*continued*)

| ID | Cal. (2σ) date /cal a BP | depth/m | Depth to consolidated substrate /m | Sample elevation & error /m, MSL | Sample type | Supporting evidence | | | | | | | Sample indicative meaning | Indicative meaning /m, MSL | RSL & range /m | Post-depositional correction for sample elevation | | | Corrected RSL & range /m, MSL |
|---|---|---|---|---|---|---|---|---|---|---|---|---|---|---|---|---|---|---|---|
| | | | | | | Features and macrofossils | Foraminifera | | | | | | | | | Compac. /m | Tectonic deformation & error/m | Ground lowering & error/m | |
| | | | | | | | Abun./g | Assemb. | Es % | B % | E % | M % | Sp. | | | | | | |
| X1-4 | 8383–8483 | 12.32 | 4.68 | −11.44 ± 0.05 | Supra tidal flat | 2.5Y 4/2 dark greyish brown, sandy silt, plant fragments, organic, interbedded sands | 6 | Ab, Am, Hg | 1 | 19 | 57 | 24 | 19 | HHW – MHHW | 2.04 ± 1.31 | −13.48 ± 1.31 | 0.48 | 0.16 ± 0.08 | 0.1 ± 0.1 | −12.73 ± 1.32 |
| X1-5 | 8778–9027 | 16.38 | 0.62 | −15.50 ± 0.05 | Supra tidal flat | 5 YR 4/2 olive grey, sandy silt, organic, interbedded sands, terrestrial gastropod opercula | ~1 | Ab, Hg, Qa, | 14 | 14 | 57 | 29 | 8 | HHW – MHHW | 2.04 ± 1.31 | −17.54 ± 1.31 | 0.07 | 0.18 ± 0.09 | 0.1 ± 0.1 | −17.19 ± 1.32 |
| Swc-1 | 5452–5882 | 1.08 | 7.32 | 2.42 ± 0.50 | Upper tidal flat | Yellowish grey sandy silt, tidal marine mollusk: Cs | 20 | Ab, Ci, Em, Pt | >3 | 5 | 60 | 35 | 12 | MHHW – MHWN | 0.49 ± 0.24 | 1.93 ± 0.55 | 0.49 | 0 ± 0.06 | 0.1 ± 0.1 | 2.52 ± 0.57 |
| Swc-2 | 6321–6716 | 2.36 | 6.04 | 1.14 ± 0.50 | Mid-lower tidal flat | Dark grey silty sand, burrows, tidal marine mollusk: Sc | 177 | Qa, Ab, Ci, Ea | <3 | 1 | 47 | 52 | 13 | MHWN – MLLW | −0.32 ± 0.57 | 1.46 ± 0.76 | 0.46 | 0 ± 0.06 | 0.1 ± 0.1 | 2.02 ± 0.77 |

**Foraminifera abbreviation:** Ab, *Ammonia beccarii* vars.; Ac, *Ammonia convexidorsa*; Ci, *Cribrononion incertum*; Cs, *Cribrononion subincertum*; Ea, *Elphidium advenum*; Em, *Elphidium magellanicum*; Es, *Elphidium simplex*; Hg, *Haynesina germanica*; Na, *Nonion akitaensis*; Pn, *Pseudoeponides nakazatoensis*; Pt, *Protelphidium tuberculatum*; Ps, *Pseudogyroidina sinensis*; Pv, *Pseudononionella variabilis*; Qa, *Quinqueloculina akneriana*; Qs: *Quinqueloculina seminula*; Tt, *Triloculina trigonula*. **Tidal-subtidal mollusk abbreviation:** Pl, *Potanocorbula laevis*; Mm,*Meretrix meretrix*; Ss, *Scapharca subcrenata*; Tb, *Terebra bellanodosa*; Mv, *Mactra veneriformis.* **Tidal mollusk abbreviation:** Al*, Assiminea latericea*; Cs, *Cerithidea sinensis* Dc, *Dosinia corrugate*; Sc, *Sinonovacula constricta*; Ut, *Umbonium thomasi*; Mj, *Moerella jedoensis*. **Terrestrial gastropod abbreviation:** Bf*, Bithynia fuchsiana*; Ga, *Gyraulus albu*; Po, *Pseudamnicola opima.*

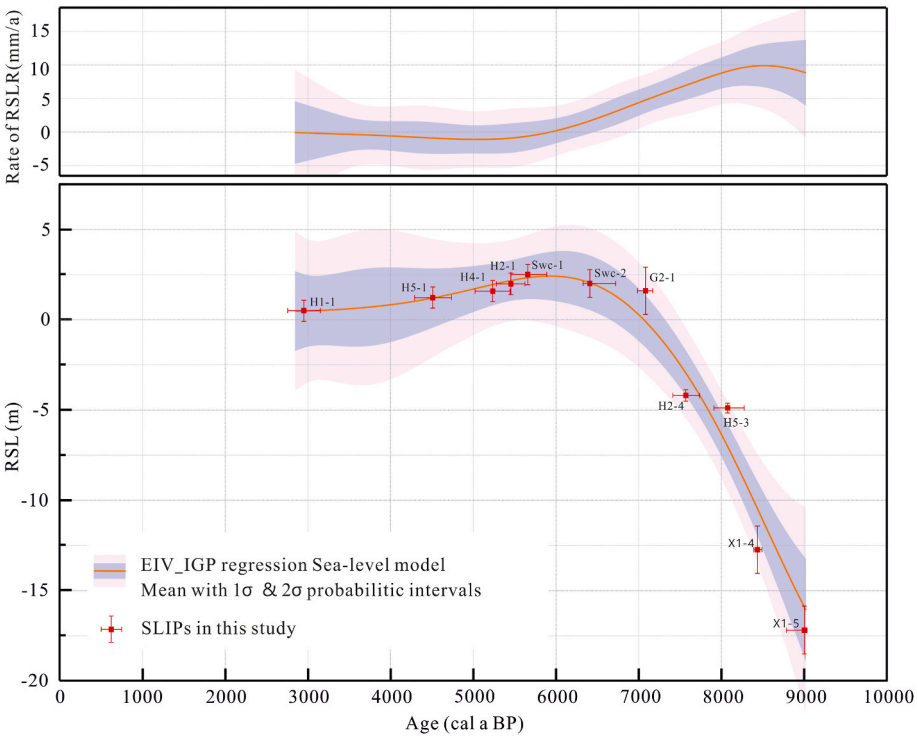


**Fig. 4.** The upper panel shows the rates of sea-level change calculated through the EIV_IGP regression sea-level model. The lower panel indicates the elevations of the SLIPs and the modeled RSL changes. The tectonic, sediment compaction and land subsidence factors have been corrected. Detailed data for SLIPs are available in Table 5.

the youngest SLIP, ID. H1-1 (Table 5), with the falling rate close to 0 mm/a (Fig. 4).

## 5. Discussion

### 5.1. RSL records along non-deltaic regions of the north and east China coasts

Considering that RSL histories in deltaic areas can be affected by long-term subsidence processes associated with sediment loading and

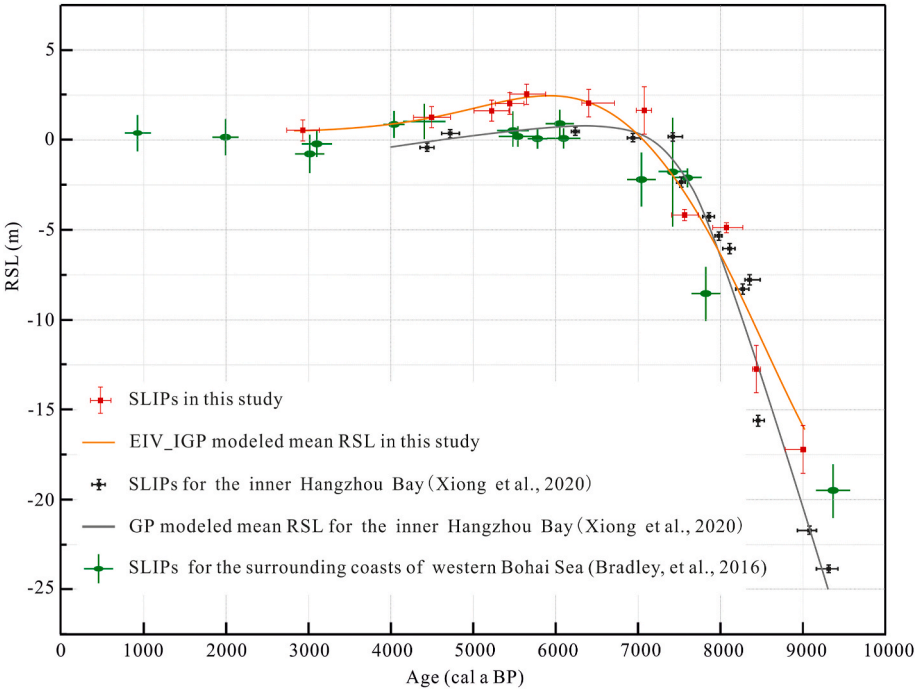


**Fig. 5.** RSL records for the southern Bohai Sea coast and its comparisons from the inner Hangzhou Bay and the surrounding coasts of western Bohai Sea.

consolidation (Zong, 2004; Bradley et al., 2016), we selected SLIPs from non-deltaic regions, including the surrounding coasts of western Bohai Sea (Bradley et al., 2016) and the inner Hangzhou Bay (Xiong et al., 2020) (see positions in Fig. 1a), for comparison with our results (Fig. 5).

The reconstructed RSL from the inner Hangzhou Bay shows a continuous rise with a gradual decreasing rate between c. 10,000 and 7000 cal a BP. By c. 6500 cal. a BP, it rose to 0.8 ± 1.4 m MSL, followed by a gradual fall to the present height around 4500 cal a BP P (Xiong et al., 2020). Two periods of accelerated sea-level rise around 8200 and 7500 cal a BP were identified in the inner Hangzhou Bay (Xiong et al., 2020), which correspond to reported periods of accelerated sea-level rise: a well-established multi-meter jump occurring around 8500–8200 cal a BP associated with the 8.2 kyr cooling event globally (e.g., Hijma and Cohen, 2010, 2019; Wang et al., 2013; Rush et al., 2023) and a more debated one between 7600 and 7400 cal a BP (e.g., Blanchon and Shaw, 1995; Yu et al., 2007) that was not identified in a high-resolution near-field dataset (e.g., Hijma and Cohen, 2019).

RSL records from study area broadly match well with those from the inner Hangzhou Bay for the period from c. 9000 to 3000 cal a BP; however, they remain slightly higher except for a short period of overlapping data around 8000–7500 cal a BP. Given that all possible local and tectonic contributions were carefully accounted for in the RSL reconstructions at both sites, the elevation differences may reflect varying levering effects across different far-field regions. Thus, the consistently higher elevations of SLIPs along the southern Bohai Sea coast from the early to mid-Holocene likely demonstrate a more significant and sustained continental levering effect. Due to the lower limited data density, periods of accelerated sea-level rise are less conclusive in the results (Fig. 5).

The Holocene RSL record from the surrounding coasts of western Bohai Sea briefly overlaps with our SLIPs, showing a rapid rise history in the early Holocene, followed by a marked slowdown as RSL approached present-day levels around 7000 cal a BP (Fig. 5). Some SLIPs from this area are approximately 1–2 m lower between 8000 and 5000 cal a BP than those in the study area, yet they still suggest a minor RSL highstand of about 0–2 m within error margins during the mid-Holocene (Bradley et al., 2016) (Fig. 5). The SLIPs from the surrounding coasts of western Bohai Sea were derived from numerous published results from the 1980s–1990s (Bradley et al., 2016). Although these SLIPs were carefully selected to avoid the paleo-Yellow River delta region, their tectonic and local signals cannot be ignored: samples were collected from locations across a 300 km range with diverse tectonic settings and varying thicknesses of compressible sediments. More importantly, they experienced different extents of modern subsidence, with cumulative subsidence between 0.6 and 2 m in this region, as documented by Su et al. (2021). Therefore, the varying discrepancies in RSL between these two sites cannot be attributed solely to different levering effects.

### 5.2. Data-model comparison

RSL change at a specific location is the sum of local, regional, and global processes across various spatial and temporal scales (e.g., Khan et al., 2019). Hence, after accounting for potential local and tectonic influences, the RSL data can provide insights into regional and global processes such as GIA and ESL. When comparing the RSL history from this study with outputs from GIA models, including ICE6G (Argus et al., 2014; Peltier et al., 2015), ANU (Lambeck et al., 2014), and the 'final model' (Bradley et al., 2016) in the Bohai Sea region (Fig. 6), several key points emerge.

In the ICE6G model, the projected RSL rose rapidly from about −3.5 m at 9000 cal a BP to 1.5 m at 8000 cal a BP, then gradually slowed and stabilized at about 4.5 m during 7000–6000 cal a BP, followed by a gradual fall until the present (Wang et al., 2020). The ICE6G model predicted early-Holocene RSL to be 5–12 m higher than the reconstructed RSL, and its prediction for the mid-Holocene highstand was also 2–4 m higher (Fig. 6). This significant mismatch between reconstructed RSL and ICE6G model outputs is observed not only in the study area but also at other locations across East and South China coasts (Xiong et al., 2018, 2020; Yu et al., 2023).

The ANU model's RSL predictions (Wang et al., 2020) suggest that early-Holocene RSL rose rapidly from about −12.5 m at 9000 cal a BP to −2.5 m around 8000 cal a BP, and to 2 m near 7000 cal a BP. Unlike the ICE-6G model, the ANU model projects lower early-Holocene RSL levels, a later onset of slowdown (7000 cal a BP versus 8000 cal a BP), and a highstand in RSL at a similar height but occurring later (~6500–6000 cal a BP versus ~7000–6000 cal a BP). Despite a significant reduction in misfit, it consistently predicts RSL to be 2–4 m higher than the reconstructed results from ~9000 to 3000 cal a BP.

The improved 'final model', which integrates an optimized ESL scenarios with a region-specific weak upper mantle Earth model, significantly reduces the predicted highstand along the China coasts (Bradley et al., 2016). This model predicts a rapid RSL rise from about

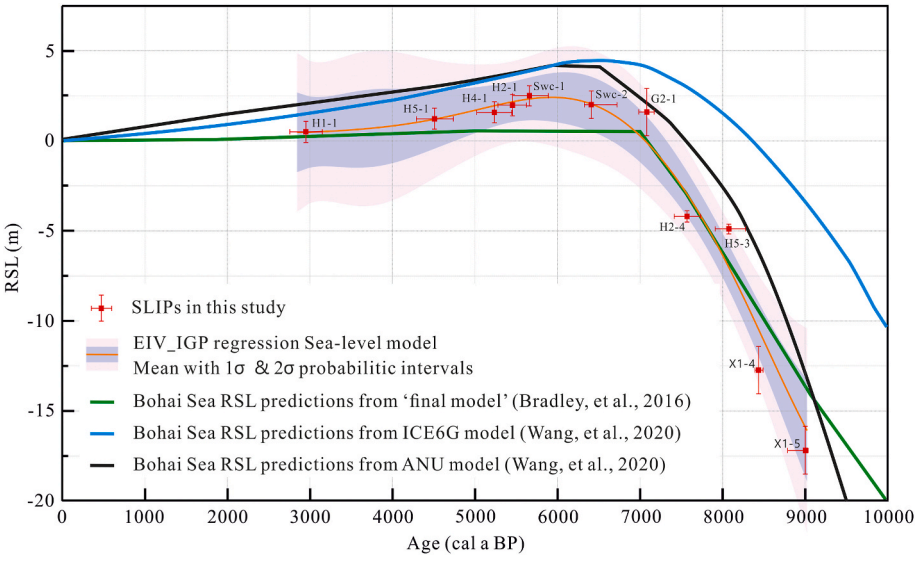


**Fig. 6.** Comparisons of RSL reconstruction (this study) with the RSL predictions from the 'final model' (Bradley et al., 2016), and two GIA models with ICE6G and ANU (Wang et al., 2020). Lithospheric thickness (km): 90 (ICE6G), 65 (ANU), 96 ('final model'); upper mantle viscosity (Pa s): 0.5 × $10^{21}$ (ICE6G, ANU), 0.05 × $10^{21}$('final model'); lower mantle viscosity (Pa s): 3.2 × $10^{21}$ (ICE6G), 10 × $10^{21}$ (ANU), 1 × $10^{21}$('final model').

−13.5 m at 9000 cal a BP to near present-day levels by 7000 cal a BP, followed by a minimal highstand of ~0.5 m between 7000 and 5000 cal a BP (Bradley et al., 2016) (Fig. 4). The sea-level records in this study align more closely with these predictions. Nevertheless, some minor data-model misfits are observed in the early Holocene, moreover, a more pronounced and higher highstand than model projections suggest in the middle Holocene.

In the early Holocene, the reconstructed RSL is 0–2 m lower than 'final model' predictions from 9000 to 8000 cal a BP, which aligns well from 8000 to 7000 cal a BP (Fig. 6). The RSL reconstruction using the EIV-IPG regression method provides a smoothed signal of sea-level changes. Consequently, when specific SLIPs, such as X1-4 and X1-5, are compared with 'final model' predictions, these discrepancies become more pronounced. As previously discussed, early Holocene RSL likely includes two periods of accelerated sea-level rise during ~8500–8200 cal a BP and 7600–7500 cal a BP. However, these periods have not been directly embedded into existing ice-melting models used for RSL predictions, including the 'final model', the ICE6G model, or the ANU model. The rapid sea-level rise associated with these periods, particularly the one with multi-meter jump around 8500–8200 cal a BP linked to the 8.2 kyr cooling event (e.g., Hijma and Cohen, 2010, 2019), can diverge from the average increase projected based on long-term global ice melting histories.

A highstand in RSL underscores the data-model misfits between 7000 and 4000 cal a BP, with our reconstructed RSL maintaining a highstand of about 1–2 m (peaking at 2.44 ± 1.34 m MSL around 6000 cal a BP), which is notably higher than the minimal highstand of ~0.5 m in the 'final model' predictions. The 'final model' assumes an initial slowdown in ESL rise at 7000 cal a BP coinciding with the final deglaciation of the Laurentide ice sheet, followed by a continued deceleration from 5000 cal a BP until melting ceased at 1000 cal a BP, resulting in a total ESL rise of 5.8 m since the 7000 cal a BP slowdown. Specifically, to reduce the predicted highstand for the Bohai Sea region, the 'final model' incorporates a lithospheric thickness of 96 km, a lower mantle viscosity of $1 \times 10^{21}$ Pa s, and an extremely weak upper mantle viscosity of $0.05 \times 10^{21}$ Pa s.

Indeed, geological data from North China indicate significant lithospheric thinning and destruction in the BSB (Chen et al., 2008; Zhu et al., 2011). The Bohai Sea region is characterized by a relatively thin lithosphere, estimated to be 65–110 km thick (e.g., Xu, 2001; Liu et al., 2016), with a strong crust but a weak upper mantle lithosphere (e.g., Liu et al., 2016). While the big low-viscosity mantle wedge and vigorous convection are known to extend beneath the central BSB (Liu et al., 2016), seismic tomographic images reveal that the Pacific stagnant slab in the mantle transition zone terminates near 120°E (Li and van der Hilst, 2010), one degree east of the study area in longitude. Moreover, the southern Bohai Sea coast is latitudinally located at the southeastern end of the BSB, where mantle convection may be subdued. This inference is supported by evidence of significant decrease of mantle heat flow in the study area and the nearby Shandong Peninsula area, comparing to the central BSB (Liu et al., 2016; Jiang et al., 2019). The specific geological setting for the southern Bohai Sea coast, characterized by the western end of the stagnant Pacific slab and the southeastern end of the BSB, likely contributes to a comparatively strong upper mantle compared to the weaker-viscosity regions along the East China coasts, which are influenced by mantle wedges or subducted slabs.

Consequently, as the rate of ESL rise slowed after 7000 cal a BP, with ~5 m of meltwater still contributing to ocean volumes (e.g., Lambeck et al., 2014; Bradley et al., 2016), the potentially strong upper mantle beneath the southern Bohai Sea coast likely induced a pronounced continental levering effect. This response of the solid Earth contributed significantly to the distinct mid-Holocene highstand observed in the southern Bohai Sea region.

## 6. Conclusions

On the southern Bohai Sea coast, the Pleistocene base slopes northward in elevation. Above this slope, a set of Holocene marine-related archives have been uncovered in a transgressive-regressive sequence. A total of 11 SLIPs have been identified within the transgressive supratidal and upper-tidal flat facies, as well as the regressive mid-lower tidal flat facies. All SLIPs have been corrected for sedimentary elevations by possible self-compaction, long-term tectonic effect, and the lowering effect due to water extraction. Consequently, the RSL history was reconstructed accordingly.

The initial seawater intrusion into this area commenced at approximately 9000 cal a BP. Until around 7000 cal a BP, the RSL experienced a rapid increase from about −17.19 ± 1.32 m to 1.62 ± 1.32 m MSL. The rates of RSL rise were very high during 9000 to 8000cal a BP, around 8–10 mm/a, but decreased rapidly after 8000 cal a BP, reaching ~4 mm/a by 7000 cal a BP. The RSL rose continuously and reached its highest highstand of 2.44 ± 1.34 m MSL around 6000 cal a BP. Subsequently, there was a distinct decline in RSL, with a maximum falling rate of 1.2 mm/a around 5000 cal a BP. After 3000–4000 cal a BP, the rate of RSL fall became very weak, close to 0 mm/a.

This RSL history supports a more significant and long-term GIA continental levering effect on the southern Bohai Sea coast compared to other non-deltaic regions along the North and East China coasts. When compared with various GIA model predictions, the reconstructed RSL in this study closely matches the 'final model' by Bradley et al. (2016). However, there are slight deviations in the results. The early Holocene data-model misfits imply long-term average ice melting trends as inputs for GIA predictions can underestimate the melting contributions during 9000 to 8000 cal a BP, highlighting the need to integrate accelerated sea-level rise events into models. The more pronounced mid-Holocene highstand observed between 7000 and 4000 cal a BP in this study may suggest the presence of a relatively strong upper mantle beneath the southern Bohai Sea coast, situated at the western end of the stagnant Pacific slab and the southeastern boundary of the BSB, rather than the extremely weak upper mantle assumed for the Bohai region in the 'final model'.

## Declaration of competing interest

The authors declare that they have no known competing financial interests or personal relationships that could have appeared to influence the work reported in this paper.

## Acknowledgments

The study was supported for design and research by the Major Program of the National Science Foundation of China (Grant No. 42293261) and CGS Project No. DD20189506. The authors are grateful to Xingyu Jiang and Yongsheng Chen, who helped with fieldwork and lab sampling. We greatly appreciate Riccardo E. M. Riva (TU Delft) for his handling and thoughtful suggestions in the GIA discussion part.

## Appendix B. Supplementary data

Supplementary data to this article can be found online at https://doi.org/10.1016/j.quascirev.2024.109166.

## References

Allen, M.B., Macdonald, D.I.M., Xun, Z., Vincent, S.J., Brouet-Menzies, C., 1997. Early Cenozoic two-phase extension and late Cenozoic thermal subsidence and inversion of the Bohai Basin, northern China. Mar. Petrol. Geol. 14 (7–8), 951–972. https://doi.org/10.1016/S0264-8172(97)00027-5.

Argus, D.F., Peltier, W.R., Drummond, R., Moore, A.W., 2014. The Antarctica component of postglacial rebound model ICE-6G_C (VM5a) based on GPS positioning, exposure

age dating of ice thicknesses, and relative sea level histories. Geophys. J. Int. 198, 537–563. https://doi.org/10.1093/gji/ggu140.
Bard, E., Hamelin, B., Delanghe-Sabatier, D., 2010. Deglacial meltwater pulse 1B and younger dryas sea levels revisited with boreholes at tathiti. Nature 327, 1235–1237, 10.1038/nature08275.
Bentley, M.J., Cofaigh, C.O., Anderson, J.B., Conway, H., Davies, B., Graham, A.G.C., Hillenbrand, C.D., Hodgson, D.A., Jamieson, S.S.R., Larter, R.D., Mackintosh, A., Smith, J.A., Verleyen, E., Ackert, R.P., Bart, P.J., Berg, S., Brunstein, D., Canals, M., Colhoun, E.A., Crosta, X., Dickens, W.A., Domack, E., Dowdeswell, J.A., Dunbar, R., Ehrmann, W., Evans, J., Favier, V., Fink, D., Fogwill, C.J., Glasser, N.F., Gohl, K., Golledge, N.R., Goodwin, I., Gore, D.B., Greenwood, S.L., Hall, B.L., Hall, K., Hedding, D.W., Hein, A.S., Hocking, E.P., Jakobsson, M., Johnson, J.S., Jomelli, V., Jones, R.S., Klages, J.P., Kristoffersen, Y., Kuhn, G., Leventer, A., Licht, K., Lilly, K., Lindow, J., Livingstone, S.J., Masse, G., McGlone, M.S., McKay, R.M., Melles, M., Miura, H., Mulvaney, R., Nel, W., Nitsche, F.O., O'Brien, P.E., Post, A.L., Roberts, S. J., Saunders, K.M., Selkirk, P.M., Simms, A.R., Spiegel, C., Stolldorf, T.D., Sugden, D. E., van der Putten, N., van Ommen, T., Verfaillie, D., Vyverman, W., Wagner, B., White, D.A., Witus, A.E., Zwartz, D., Consortium, R., 2014. A community-based geological reconstruction of antarctic ice sheet deglaciation since the last glacial maximum. Quat. Sci. Rev. 100, 1–9. https://doi.org/10.1016/j.quascirev.2014.06.025.
Blanchon, P., Shaw, J., 1995. Reef drowning during the last deglaciation: evidence for catastrophic sea-level rise and ice-sheet collapse. Geology 23 (1), 4–8. https://doi.org/10.1130/0091-7613(1995)023<0004:RDDTLD>2.3.CO;2.
Bradley, S.L., Milne, G.A., Horton, B.P., Zong, Y., 2016. Modelling sea level data from China and Malay-Thailand to estimate Holocene ice-volume equivalent sea level change. Quat. Sci. Rev. 137, 54–68. https://doi.org/10.1016/j.quascirev.2016.02.002.
Cahill, N., Kemp, A.C., Horton, B.P., Parnell, A.C., 2015. Modeling sea-level change using errors-in-variables integrated Gaussian processes. Ann. Appl. Stat. 9 (2), 547–571. https://doi.org/10.1214/15-AOAS824.
Cahill, N., Kemp, A.C., Horton, B.P., Parnell, A.C., 2016. A Bayesian hierarchical model for reconstructing relative sea level: from raw data to rates of change. Clim. Past 12 (2), 525–542. https://doi.org/10.5194/cp-12-525-2016.
Chen, Q.Q., Zhu, Y.R., 2012. Holocene evolution of bottom sediment distribution on the continental shelves of the Bohai Sea, Yellow Sea and east China sea. Sediment. Geol. 273–274, 58–72. https://doi.org/10.1016/j.sedgeo.2012.06.011.
Chen, L., Tao, W., Zhao, L., Zheng, T.Y., 2008. Distinct lateral variation of lithospheric thickness in the Northeastern North China Craton. Earth Planet Sci. Lett. 267, 56–68. https://doi.org/10.1016/j.epsl.2007.11.024.
Clark, P.U., Mix, A.C., 2002. Ice sheets and sea level of the last glacial maximum. Quat. Sci. Rev. 21, 1–7. https://doi.org/10.1016/S0277-3791(01)00118-4.
Guo, Y., Mao, L., Zhu, L., Mo, D., 2022. Environmental evolution and human adaption recorded from a salt production site at the coastal plain of Laizhou bay, China. Front. Mar. Sci. 9, 873220. https://doi.org/10.3389/fmars.2022.873220.
Hanebuth, T., Stattegger, K., Grootes, P.M., 2000. Rapid flooding of the Sunda Shelf: a late-glacial sea-level record. Science 288, 1033–1035. https://doi.org/10.1126/science.288.5468.1033.
Heaton, T.J., Kohler, P., Butzin, M., Bard, E., Reimer, R.W., Austin, W.E.N., Ramsey, C.B., Grootes, P.M., Hughen, K.A., Kromer, B., 2020. Marine20—the marine radiocarbon age calibration curve (0–55,000 cal BP). Radiocarbon 62, 779–820. https://doi.org/10.1017/RDC.2020.68.
Hijma, M.P., Cohen, K.M., 2010. Timing and magnitude of the sea-level jump preluding the 8200 yr event. Geology 38 (1), 275–278. https://doi.org/10.1130/G30439.
Hijma, M.P., Cohen, K.M., 2019. Holocene sea-level database for the Rhine-Meuse Delta, The Netherlands: implications for the pre-8.2 ka sea-level jump. Quat. Sci. Rev. 214, 68–86. https://doi.org/10.1016/j.quascirev.2019.05.001.
Hijma, M.P., Engelhart, S.E., Tornqvist, T.E., Horton, B.P., Hu, P., Hill, D.F., 2015. A protocol for a geological Sea-Level database. Handbook of Sea-Level Research. John Wiley & Sons, Ltd, pp. 536–553. https://doi.org/10.1002/9781118452547.ch34.
Horton, B.P., Gibbard, P.L., Mine, G.M., Morley, R.J., Purintavaragul, C., Stargardt, J.M., 2005. Holocene sea levels and palaeoenvironments, Malay-Thai Peninsula, southeast Asia. Holocene 15, 1199–1213. https://doi.org/10.1191/0959683605hl891rp.
Hu, S., O'Sullivan, P.B., Raza, A., Kohn, B.P., 2001. Thermal history and tectonic subsidence of the Bohai Basin, northern China: a Cenozoic rifted and local pull-apart basin. Phys. Earth Planet. In. 126 (3–4), 221–235. https://doi.org/10.1016/S0031-9201(01)00257-6.
Huang, L., Liu, C., Wang, Y., Zhao, J., Mountney, N.P., 2014. Neogene-Quaternary postrift tectonic reactivation of the Bohai Bay Basin, eastern China. AAPG (Am. Assoc. Pet. Geol.) Bull. 98 (7), 1377–1400. https://doi.org/10.1306/03071413046.
Jiang, G., Hu, S., Shi, Y., Zhang, C., Wang, Z., Hu, D., 2019. Terrestrial heat flow of continental China: updated dataset and tectonic implications. Tectonophysics 753, 36–48. https://doi.org/10.1016/j.tecto.2019.01.006.
Khan, N.S., Horton, B.P., Engelhart, S., Rovere, A., Vacchi, M., Ashe, E.L., Törnqvist, T.E., Dutton, A., Hijma, M.P., Shennan, I., the HOLSEA working group, 2019. Inception of a global atlas of sea levels since the Last Glacial Maximum. Quat. Sci. Rev. 220, 359–371. https://doi.org/10.1016/j.quascirev.2019.07.016.
Lambeck, K., Yokoyama, Y., Purcell, T., 2002. Into and out of the Last Glacial Termination: sea level change during oxygen isotope stages 3 and 2. Quat. Sci. Rev. 21, 343–360. https://doi.org/10.1016/S0277-3791(01)00071-3.
Lambeck, K., Rouby, H., Purcell, A., Sun, Y.Y., Sambridge, M., 2014. Sea level and global ice volume from the last glacial maximum to the Holocene. Proc. Natl. Acad. Sci. USA 111, 15296–15303. https://doi.org/10.1073/pnas.1411762111.
Li, C., van der Hilst, R.D., 2010. Structure of the upper mantle and transition zone beneath Southeast Asia from traveltime tomography. J. Geophys. Res. Solid Earth 115, 19. https://doi.org/10.1029/2009JB006882.
Li, J., Shang, Z., Wang, H., Pei, Y., Wang, F., Tian, L., 2010. Modern foraminifera assemblages: vertical zonation and its indication for Holocene sea level and geoenvironmental reconstruction in Bohai Bay, China. Geol. Bull. China 29 (5), 650–659. https://doi.org/10.3969/j.issn.1671-2552.2010.05.003 (in Chinese with English abstract).
Li, J., Shang, Z., Jiang, X., Chen, Y., Wang, F., Tian, L., Wang, H., 2016. Sea-level indicated by foraminifera assemblages living in the open muddy flats with or without influence of the chenier ridges in Bohai Bay coastal areas. Geol. Bull. China 35 (10), 1578–1583. https://doi.org/10.3969/j.issn.1671-2552.2016.10.003 (in Chinese with English abstract).
Liu, J.P., Milliman, J.D., Gao, S., Cheng, P., 2004. Holocene development of the Yellow River's subaqueous delta, North Yellow sea. Mar. Geol. 209, 45–67. https://doi.org/10.1016/j.margeo.2004.06.009.
Liu, J., Saito, Y., Wang, H., Yang, Z., Nakashima, R., 2007. Sedimentary evolution of the Holocene subaqueous clinoform off the Shandong Peninsula in the Yellow Sea. Mar. Geol. 236, 165–187. https://doi.org/10.1016/j.margeo.2006.10.031.
Liu, Q., Zhang, L., Zhang, C., He, L., 2016. Lithospheric thermal structure of the North China Craton and its geodynamic implications. J. Geodyn. 102, 139–150. https://doi.org/10.1016/j.jog.2016.09.005.
Liu, Q., He, L., Yi, Z., Zhang, L., 2022. Anomalous post-rift subsidence in the Bohai Bay Basin, Eastern China: contributions from mantle process and fault activity. Tectonics 41 (1), e2021TC006748. https://doi.org/10.1029/2021TC006748.
Mitrovica, J.X., Milne, G.A., 2002. On the origin of late Holocene Sea-level highstands within equatorial ocean basins. Quat. Sci. Rev. 21, 2179–2190. https://doi.org/10.1016/S0277-3791(02)00080-X.
Oliver, G.J.H., Terry, J.P., 2019. Relative sea-level highstands in Thailand since the Mid-Holocene based on $^{14}$C rock oyster chronology. Palaeogeogr. Palaeoclimatol. Palaeoecol. 517, 30–38. https://doi.org/10.1016/j.palaeo.2018.12.005.
Peltier, W.R., Argus, D.F., Drummond, R., 2015. Space geodesy constrains ice age terminal deglaciation: the global ICE-6G_C (VM5a) model. J. Geophys. Res. Solid Earth 120, 450–487. https://doi.org/10.1002/2014JB011176.
Qin, Y., Zhao, Y., Chen, L., Zhao, S., 1990. Geology of the Bohai Sea. Science Press, Beijing.
Reimer, P.J., Austin, W.E.N., Bard, E., Bayliss, A., Blackwell, P.G., Ramsey, C.B., Butzin, M., Cheng, H., Edwards, R.L., Friedrich, M., 2020. The IntCal20 Northern Hemisphere radiocarbon age calibration curve (0–55 cal kBP). Radiocarbon 62, 725–757. https://doi.org/10.1017/RDC.2020.41.
Rush, G., Garrett, E., Bateman, M.D., Bigg, G.R., Hibbert, F.D., Smith, D.E., Gehrels, W. R., 2023. The magnitude and source of meltwater forcing of the 8.2 ka climate event constrained by relative sea-level data from eastern Scotland. Quaternary Science Advances 12, 1–14. https://doi.org/10.1016/j.qsa.2023.100119.
Southon, J., Kashgarian, M., Fontugne, M., Metivier, B., W-S Yim, W., 2002. Marine reservoir corrections for the Indian ocean and southeast Asia. Radiocarbon 44 (1), 167–180. https://doi.org/10.1017/S0033822200064778.
Stanford, J.D., Hemingway, R., Rohling, E.J., Challenor, P.G., Medina-Elizalde, M., Lester, A.J., 2011. Sea-level probability for the last deglaciation: a statistical analysis of far-field records. Global Planet. Change 79, 193–203. https://doi.org/10.1016/j.gloplacha.2010.11.002.
Su, G., Wu, Y., Zhan, W., Zheng, Z., Chang, L., Wang, J., 2021. Spatiotemporal evolution characteristics of land subsidence caused by groundwater depletion in the North China plain during the past six decades. J. Hydrol. 600, 126678. https://doi.org/10.1016/j.jhydrol.2021.126678.
Sun, W., Zhou, X., Feng, Y., Fu, Y., 2018. Analysis on the tidal spatio-temporal characteristics in Shandong coastal areas. J. Ocean Technol. 37 (4), 68–75. https://doi.org/10.3969/j.issn.1003-2029.2018.04.011 (in Chinese with English abstract).
Tam, C.-Y., Zong, Y., Kamaludin, b.H., Hamlee, b.I., Habibah, b.J., Xiong, H., Wu, P., Sun, Y., Huang, G., Zheng, Z., 2018. A below-the-present late Holocene relative sea level and the glacial isostatic adjustment during the Holocene in the Malay Peninsula. Quat. Sci. Rev. 201, 206–222. https://doi.org/10.1016/j.quascirev.2018.10.009.
Tian, L., Wang, D., Pei, Y., Wang, F., Li, J., Shang, Z., Wang, H., 2011. Topographic and geomorphic evolution process in tianjin binhai new area after middle Holocene. North China Geol 1, 53–62. https://doi.org/10.3969/j.issn.1672-4135.2011.01.009 (in Chinese with English abstract).
Tian, L., Chen, Y., Jiang, X., Wang, F., Pei, Y., Chen, Y., Shang, Z., Li, J., Li, Y., Wang, H., 2017. Post-glacial sequence and sedimentation in the western Bohai Sea, China, and its linkage to global sea-level changes. Mar. Geol. 388, 12–24. https://doi.org/10.1016/j.margeo.2017.04.003.
Törnqvist, T.E., De Jong, A.F.M., Oosterbaan, W.A., Van der Borg, K., 1992. Accurate dating of organic deposits by AMS 14C measurement of macrofossils. Radiocarbon 34, 566–577. https://doi.org/10.1017/S0033822200063840.
Uehara, K., Saito, Y., 2003. Late Quaternary evolution of the Yellow/East China Sea tidal regime and its impacts on sediments dispersal and seafloor morphology. Sediment. Geol. 162, 25–38. https://doi.org/10.1016/S0037-0738(03)00234-3.
Vis, G.J., Cohen, K.M., Westerhoff, W.E., Veen, J.H.T., Hijma, M.P., van der Spek, A.J., Vos, P.C., 2015. Paleogeography. Handbook of Sea-level research, 514-535. https://doi.org/10.1002/9781118452547.ch33.
Wang, Z., Zhan, Q., Long, H., Saito, Y., Gao, X., Wu, X., Li, L.I.N., Zhao, Y., 2013. Early to mid-Holocene rapid sea-level rise and coastal response on the southern Yangtze delta plain, China. J. Quat. Sci. 28 (7), 659–672. https://doi.org/10.1002/jqs.2657.
Wang, F., Li, J., Chen, Y., Fang, J., Zong, Y., Shang, Z., Wang, H., 2015. The record of mid-Holocene maximum landward marine transgression in the west coast of Bohai Bay, China. Mar. Geol. 359, 89–95. https://doi.org/10.1016/j.margeo.2014.11.013.

Wang, F., Zong, Y., Mauz, B., Li, J., Fang, J., Tian, L., Chen, Y., Shang, Z., Jiang, X., Spada, G., Melini, D., 2020. Holocene sea-level change on the central coast of Bohai Bay, China. Earth Surf. Dyn. 8, 679–693. https://doi.org/10.5194/esurf-8-679-2020.

Wang, F., Hu, Y., Tian, L., Shi, P., Li, J., Chen, Y., Li, Y., Shang, Z., Jiang, X., Yuan, H., Yang, P., Wen, M., Zhao, Y., Yang, Y., Wang, H., 2024. Sea level change in Bohai bay. North China Geology 47 (1), 1–20. https://doi.org/10.19948/j.12-1471/P.2024.01.01 (in Chinese with English abstract).

Xiong, H., Zong, Y., Qian, P., Huang, G., Fu, S., 2018. Holocene sea-level history of the northern coast of South China Sea. Quat. Sci. Rev. 194, 12–26. https://doi.org/10.1016/j.quascirev.2018.06.002.

Xiong, H., Zong, Y., Li, T., Long, T., Huang, G., Fu, S., 2020. Coastal GIA processes revealed by the early to middle Holocene sea-level history of east China. Quat. Sci. Rev. 233, 106249. https://doi.org/10.1016/j.quascirev.2020.106249.

Xu, Y.G., 2001. Thermo-tectonic destruction of the Archaean lithospheric keel beneath the Sino-Korean craton in China: evidence, timing and mechanism. Phys. Chem. Earth Part A 26, 747–757. https://doi.org/10.1016/S1464-1895(01)00124-7.

Xu, X., Bai, L., Wei, L., Chen, G., Yu, G., 2019. Discussion on initiation time of the latest tectonic movement in break-up region of the North China craton. Earth Sci. 44 (5), 1647–1660. https://doi.org/10.3799/dqkx.2019.978.

Xue, C., 1993. Historical changes in the Yellow River delta, China. Mar. Geol. 113, 321–330. https://doi.org/10.1016/0025-3227(93)90025-Q.

Xue, C., Ding, D., 2008. Weihe River-mihe River Delta in south coast of Bohai Sea, China: sedimentary sequence and architecture. Sci. Geogr. Sin. 28 (5), 672–676. https://doi.org/10.3969/j.issn.1000-0690.2008.05.014 (in Chinese with English abstract).

Yao, Z., Shi, X., Li, X., Liu, Y., Liu, J., Qiao, S., Bai, Y., Wang, X., 2017. Sedimentary environment and paleo-tidal evolution of the eastern Bohai Sea, China since the last glaciation. Quat. Int. 440, 129–138. https://doi.org/10.1016/j.quaint.2016.04.010.

Yi, L., Deng, C.L., Tian, L.Z., Xu, X.Y., Jiang, X.Y., Qiang, X.K., Qin, H.F., Ge, J.Y., Chen, G.Q., Su, Q., Chen, Y.P., Shi, X.F., Xie, Q., Yu, H.J., Zhu, R.X., 2016. Plio-pleistocene evolution of Bohai basin (East Asia): demise of Bohai paleolake and transition to marine environment. Sci. Rep. 6 (1), 29403. https://doi.org/10.1038/srep29403.

Yu, S.-Y., Berglund, B.E., Sandgren, P., Lambeck, K., 2007. Evidence for a rapid sea-level rise 7600 yr. ago. Geology 35, 891–894. https://doi.org/10.1130/G23859A.1.

Yu, F., Li, N., Tian, G., Huang, Z., Xiong, H., Li, T., Liu, S., Liu, Y., 2023. A re-evaluation of Holocene relative sea-level change along the Fujian coast, southeastern China. Palaeogeogr. Palaeoclimatol. Palaeoecol. 622, 111577. https://doi.org/10.1016/j.palaeo.2023.111577.

Zhang, J., Wang, J., 1999. Combined impacts of MSL rise and the enlarged tidal range on the engineering design standard in the areas around the Huanghe River mouth. Mar. Sci. Bull. 18, 1–9. https://doi.org/10.3969/j.issn.1001-6392.1999.05.001 (in Chinese with English abstract).

Zhu, Y.R., Chang, R.F., 2000. Preliminary study of the dynamic origin of the distribution pattern of bottom sediments on the continental shelves of the Bohai Sea, Yellow Sea and East China Sea. Estuar. Coast Shelf Sci. 51, 663–680. https://doi.org/10.1006/ecss.2000.0696.

Zhu, R.X., Chen, L., Wu, F.Y., Liu, J.L., 2011. Timing, scale and mechanism of the destruction of the North China Craton. Sci. China Earth Sci. 54, 789–797. https://doi.org/10.1007/s11430-011-4203-4.

Zong, Y., 2004. Mid-Holocene sea-level highstand along the southeast coast of China. Quat. Int. 117, 55–67. https://doi.org/10.1016/S1040-6182(03)00126-0.